Supporting Information

Pangalos et al. 10.1073/pnas.1215496110

SI Materials and Methods

Slice Processing and Anatomical Reconstruction. Cells were routinely loaded with 0.3–0.5% biocytin. After recordings, slices were transferred to 4% paraformaldehyde. Slices were resectioned (100 μm). Biocytin-filled cells were subsequently visualized with 3,3′-diaminobenzidine tetrahydrochloride (0.015%) using a standard ABC kit (Vectorlabs) and reconstructed on a light microscope at 60× or 100× with a Neurolucida 3D reconstruction system (MicroBrightField).

Data Analysis. Data analysis was done using custom-made code in Matlab (MathWorks, Natick, MA). The following intrinsic cellular parameters were determined: Resting membrane potential was estimated as the initial membrane potential recorded in the current-clamp configuration after rupturing the cell membrane. For estimation of the cell's input resistance, R_i, we applied repeated voltage steps of 50-ms duration. The voltage step ΔV (4 mV) was then divided by the current difference ΔI (mean steady-state current minus mean baseline current) in the respective experiment. We estimated the SEM of ΔI by error propagation of the SEMs of both baseline and steady-state estimates. To ensure a reliable R_i estimation, we considered only those measurements in which the relative error of ΔI (i.e., SEM/ΔI) did not exceed 15%. To avoid the inclusion of spontaneous synaptic inputs in the measurements and maximize the reliability of R_i estimation, we used a window of variable size (5, 10, 15, ..., 40 ms). The action potential threshold was determined by injecting the lowest possible current to elicit spikes during characterization of the cells' intrinsic properties (rheobase). The threshold was defined as the voltage where $dV/dt \sim 20$ mV/ms.

Sharp wave-ripple (SWR) detection was realized using a threshold-based algorithm, as described (1). After detection, SWR-associated intracellular traces [±100 ms aligned to the maximum of the local field potential (LFP) SWR] were baseline-corrected by subtracting their respective means. For the estimation of synaptic input during SWRs, we chose the average current rather than total charge transfer (Fig. S1). The following algorithm was used: First, in each experiment, a threshold was defined as 1× the averaged SD of all baseline shift-corrected current traces; other threshold levels did not change main results on the distinction between participating and silent oriens-lacunosum-moleculare (O-LM) cells (Fig. S1*B*). Subsequently, for each individual trace, a 100-ms window of interest was determined from −50 ms to +50 ms with respect to the peak of the extracellularly identified SWR. To determine the times at which the input crosses the threshold, currents within this window were rectified and smoothed (moving average filter with a 10-ms window). The time interval between threshold crossings was defined as the width Δt of the input. The average synaptic input current for individual ripples was quantified by dividing the charge transfer (i.e., the time integral of the unprocessed currents within threshold crossings) by Δt.

Ripple amplitude of individual events was estimated as the local maximum of the envelope derived from the Hilbert transform applied on bandpass-filtered data (second order Butterworth filter with cutoff frequencies of 127–300 Hz).

Determination of phase and envelope. Each individual SWR event was band-pass filtered (127–300 Hz, second order Butterworth filter). The envelope and phase of the filtered LFP signal were further obtained by means of the Hilbert transform ("Hilbert envelope" and "Hilbert phase"). For the analysis of the phases of synaptic input, the same procedure was performed on the cPSC-derived conductance traces obtained in voltage-clamp mode.

Spike time detection. Spike times were analyzed in a time window of 120 ms length centered on the LFP ripple envelope peak. For whole-cell current-clamp data, we used a threshold algorithm to detect spikes, and spike times were determined by the maximum slope in the ascending phase. For action current spikes recorded in the cell-attached voltage-clamp configuration, we considered events only if they exceeded 4×SD of the baseline both in the raw signal and in the 0.5–1.5 kHz band. A spike time was determined by the trough of the measured current. Spike times were always measured relative to the corresponding ripple peak in the LFP.

Smoothed histogram profiles in Fig. 3*B* and Fig. S4, *C2* were obtained by replacing every spike with a Gaussian kernel (σ = 3.7 ms) and adding the kernels.

Spike phases during ripples. Spike phase was the Hilbert phase of the LFP at the time of the spike. To restrict the analysis to ripples, we considered only spikes occurring within a time window of 40 ms centered on the envelope peak; furthermore, the value of the envelope at the time of a spike had to exceed 2× the baseline value, which was estimated as the mean Hilbert envelope outside SWRs. For each cell, the degree of phase locking was quantified by the mean resultant length (vector strength) of the phase distribution.

Phase of synaptic input. For each SWR, a trace proportional to the excitatory synaptic conductance was obtained by inverting the respective cEPSC trace (see Fig. S3). Because we were interested in the temporal structure rather than the actual values of conductance, this quantity was regarded as an equivalent for the excitatory conductance throughout the text, displayed in arbitrary units (a.u.). For this analysis, we considered only those events in which the current-envelope-peak occurred within a time window of 40 ms centered on the LFP-envelope peak. This constraint allowed us to restrict the analysis to only those currents that co-occur with the LFP ripple and also assured a minimum overlap between LFP and current required for a reliable phase measurement. Based on these constraints, across recordings, 92 ± 1% of detectable currents were included into the analysis. To analyze the phase of the excitatory synaptic input with respect to the LFP, we subtracted the Hilbert phase of the conductance trace from the Hilbert phase of the LFP. The difference describes the time course of the phase of the synaptic input relative to the LFP phase. This phase difference is approximately constant at times when both LFP and current envelopes are large. The synaptic input phase was determined by the phase difference measured at the time of the maximum overlap of the two envelopes. The time of maximum overlap was defined as the mean of the peak times of voltage and current envelopes. To quantify the reliability of the phase estimation, we measured the variability of the phase difference trace around the estimated value during the time course of a ripple event. The error was defined as the root mean square of the deviations from the estimated synaptic input phase. The value of 7 ms (see Fig. S3*D*) corresponds to the time span at which both envelopes are above their half-peaks. This time span was obtained from the average current and LFP envelopes (Fig. 2*B*). In the analysis we included only those events where both, peaks of current and voltage envelopes exceeded at least 3 times their baseline values (as described in the previous section). Considering all constraints regarding time and amplitude, 76.4 ± 3.5% of all available events were analyzed (1,791 events in total). For each data set (cell) we estimated an average phase-vector that is described by its phase and vector strength [orange dots in Figs. 2*C* and 3*C*; each of these dots represents the average of one data

set (cell)]. Across cells, we determined the mean phase of vectors and the respective SEM. For the polar plots presented in Figs. 2*C* and 3*C* and Figs. S4*D*, we additionally calculated the average vector across cells (black arrows).

Spectral analysis of SWRs was computed with the Fast Fourier Transform (FFT) algorithm applied on stretches of 160 ms of raw data centered on the SWR peak. Frequency resolution of the resulting PSD plot (Fig. 1*C*) was 10 Hz.

The coherence $C_{xy}(f)$ of two signals x and y, defined as their normalized cross-spectral density, was computed using PSDs by the Welch periodogram method (2,048 FFT points).

Statistical evaluation. Data are reported as mean ± SEM, which is also indicated by error bars in the figures. Statistical significance was assessed using the rank-sum, the two-sample Kolmogorov–Smirnov (K–S) or the Kuiper's test (2) at the given significance level (P).

1. Maier N, Morris G, Johenning FW, Schmitz D (2009) An approach for reliably investigating hippocampal sharp wave-ripples in vitro. *PLoS ONE* 4(9):e6925.

2. Berens P (2009) CircStat: A MATLAB Toolbox for Circular Statistics. *J Stat Softw* 31(10): 1–21.

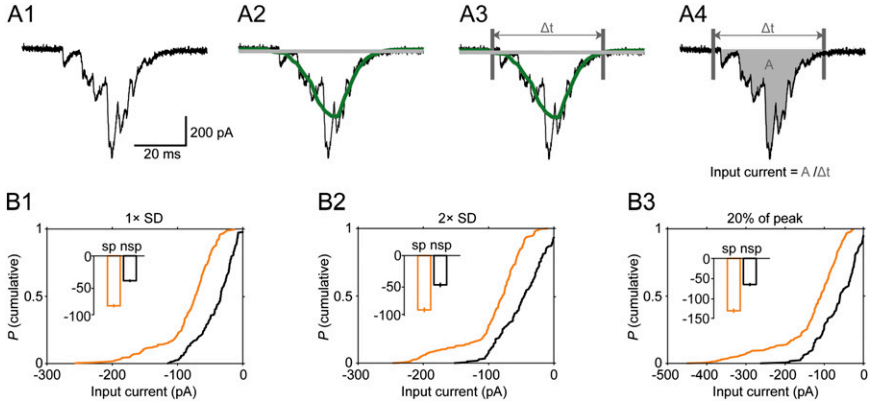

Fig. S1. Estimation of average synaptic input currents during ripples and validation of the applied threshold criterion to estimate the signal width (see also *SI Materials and Methods, Data Analysis*). (*A1*) Example of ripple-associated synaptic input in an O-LM neuron after offset correction. (*A2*) The green trace represents the inverted and smoothed (moving average filter; 10 ms time constant) version of the rectified original input current; the averaged SD of all current traces of the cell is given by the gray horizontal line. (*A3*) The width Δt of the signal was determined as the time difference of the intersections of the smoothed signal (green line) and the gray line. (*A4*) Finally, the average estimated synaptic input current is quantified by dividing the time integral of the current trace (area A under curve) by the width Δt of the signal. (*B1*) Distributions of average synaptic input currents for spiking (orange) and silent (black) O-LM neurons with 1× the averaged SD. (*Inset*) The mean values. The plot is identical to that displayed in Fig. 4*B*. The same analysis was applied on the same data but different criteria were used to determine the signal width, i.e., 2× SD (*B2*) and 20% of event peak (*B3*). For all tested thresholds, highly significant differences were found for spiking and nonspiking O-LM neurons. K–S test P values: 1.6×10^{-24} (*B1*), 5.7×10^{-18} (*B2*), and 1.0×10^{-15} (*B3*).

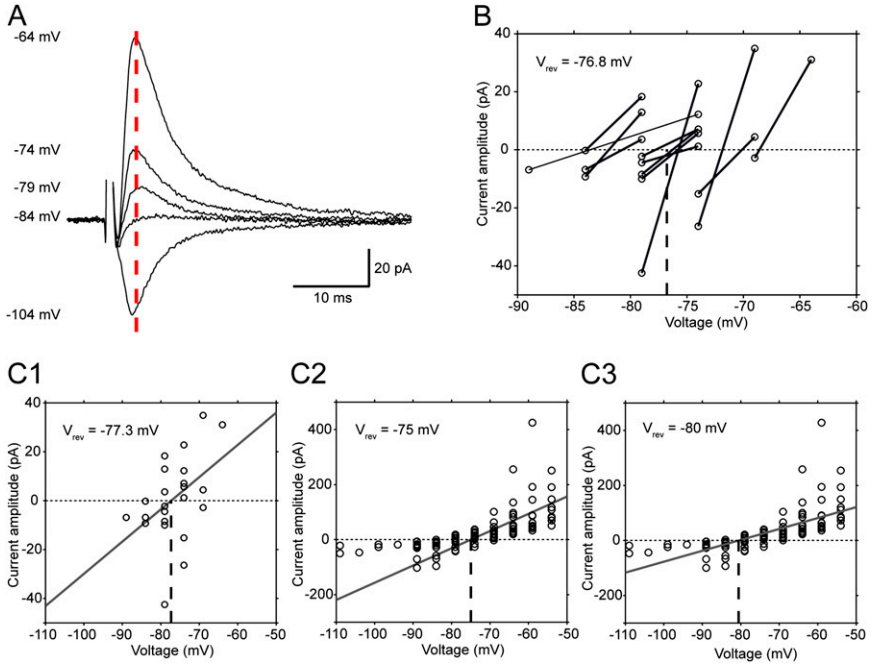

Fig. S2. Estimation of the reversal potential of inhibition in O-LM cells in area CA1. (*A*) Examples of evoked synaptic currents in an O-LM interneuron voltage-clamped at different holding potentials in the presence of antagonists at AMPA/kainite, NMDA, and $GABA_B$ receptors [20 μM 2,3-dioxo-6-nitro-1,2,3,4-tetrahydrobenzo(f)quinoxaline-7-sulfonamide (NBQX), 50 μM D-APV, and 20 μM SCH 50911]. The dashed red line refers to the time point of the signal peak at −64 mV and gives the reference at which current amplitudes were determined for other holding potentials. For display, the stimulus artifact was truncated. (*B*) The closest amplitude values below and above 0 pA were plotted against their respective holding potential (12 cells). Solid lines indicate the corresponding point-pairs. The vertical dashed line represents the mean for all zero crossings and hence, the average experimentally determined reversal potential of Cl^- (V_{rev} = −76.8 mV). (*C*) Different ways to determine the Cl^- reversal potential were additionally tested. (*C1*) The linear regression fit through the same values as shown in panel (*B*, dashed line, V_{rev} = −77.3 mV). (*C2* and *C3*) Inspection of postsynaptic current amplitudes recorded below V_{rev} demonstrated outward rectification of IPSCs in O-LM neurons. Linear regression fit through values ≥−74 mV (*C2*) and through all data points (*C3*) illustrates the bias toward negative reversal potentials by outward rectification. For this study, the method displayed in *B* was applied.

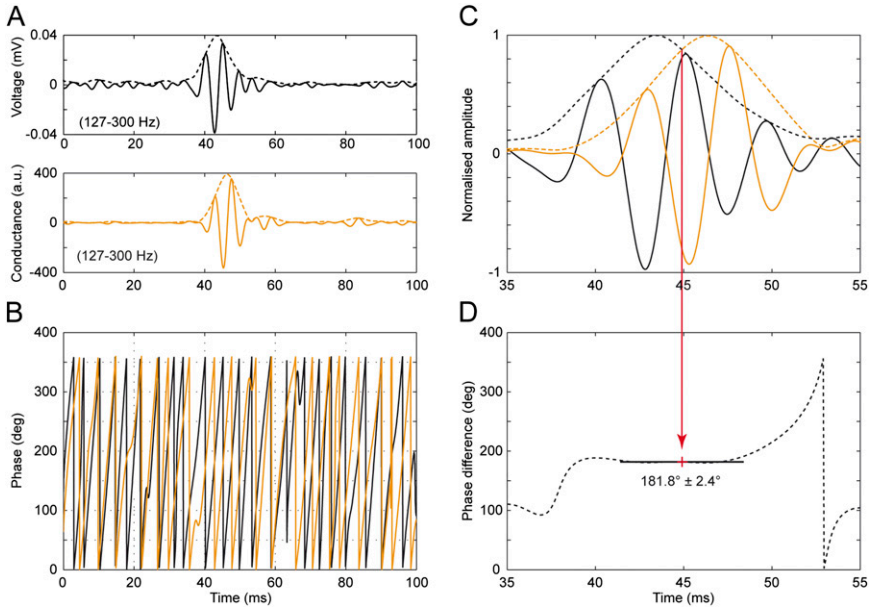

Fig. S3. Phase and envelope analysis (see also *SI Materials and Methods, Data Analysis*). (*A*) Ripple component (127–300 Hz, bandpass-filtered) of both LFP (*Upper*, black) and excitatory cPSC-derived conductance (*Lower*, orange) overlaid with the respective envelopes derived from their Hilbert transforms. (*B*) Hilbert phase of the signals shown in *A*; black: LFP; orange: conductance. (*C*) Magnification and overlay of the normalized signals shown in *A*. (*D*) Phase difference trace (dashed black line). The dashed line is obtained by subtracting the phase of the conductance (orange trace in *B*) from the phase of the LFP (black trace in *B*). The phase of synaptic input was estimated by determining the phase difference at the point of maximum envelope overlap as depicted in *C* (red arrow). The phase estimation error is obtained from the deviations of the phase trace from the sampled value within a window of 7 ms (black horizontal line). For this particular example, the phase estimate was 181.8° ± 2.4°.

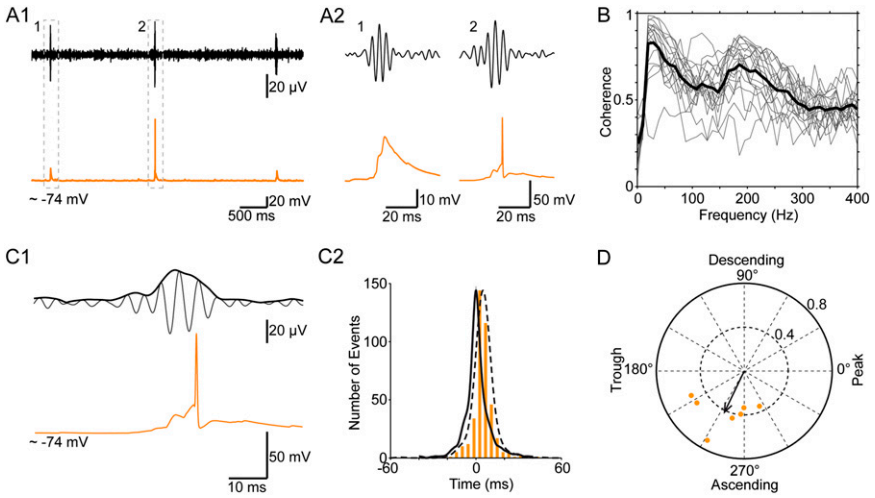

Fig. S4. Current-clamp recordings in identified O-LM neurons revealed ripple-coherent postsynaptic voltage fluctuations. (*A1 Upper*) The 127–300 Hz bandpass-filtered LFP (black). (*Lower*) Simultaneous current-clamp recording from an O-LM cell at resting membrane potential, as indicated. (*A2*) Magnification of the highlighted events shown in *A1*. (*B*) LFP ripples and their associated current-clamp equivalents were phase-locked, as indicated by a coherence peak at ~200 Hz. The black line represents the average of 18 coherence functions (gray lines) each calculated for 20 randomly picked pairs of LFP and PSP events. (*C1 Upper*) Ripple overlaid with its envelope. (*Lower*) Example of an action potential (magnified version of the data shown in *A2 Right*). (*C2*) Histogram of spike times (orange) of seven O-LM neurons with respect to the peak of each corresponding ripple envelope (average, black; arbitrary units). Overlaid histogram profile (dashed line) represents the sum of Gaussians ($\sigma = 3.7$ ms) centered on the spike times (delay of spike times with respect to the ripple maximum: 5.2 ms; SD: 6.2 ms; 401 spikes). Action potentials occurred late during ripples. (*D*) Polar phase plot indicating average firing phases for seven cells. Note that spike phases clustered to the early ascending phase of ripples. Dots illustrate the degree of phase locking (vector strength) of the phase distribution; circles and numbers in black indicate the calibration of vector strength; average vector: 244°, vector strength: 0.41.

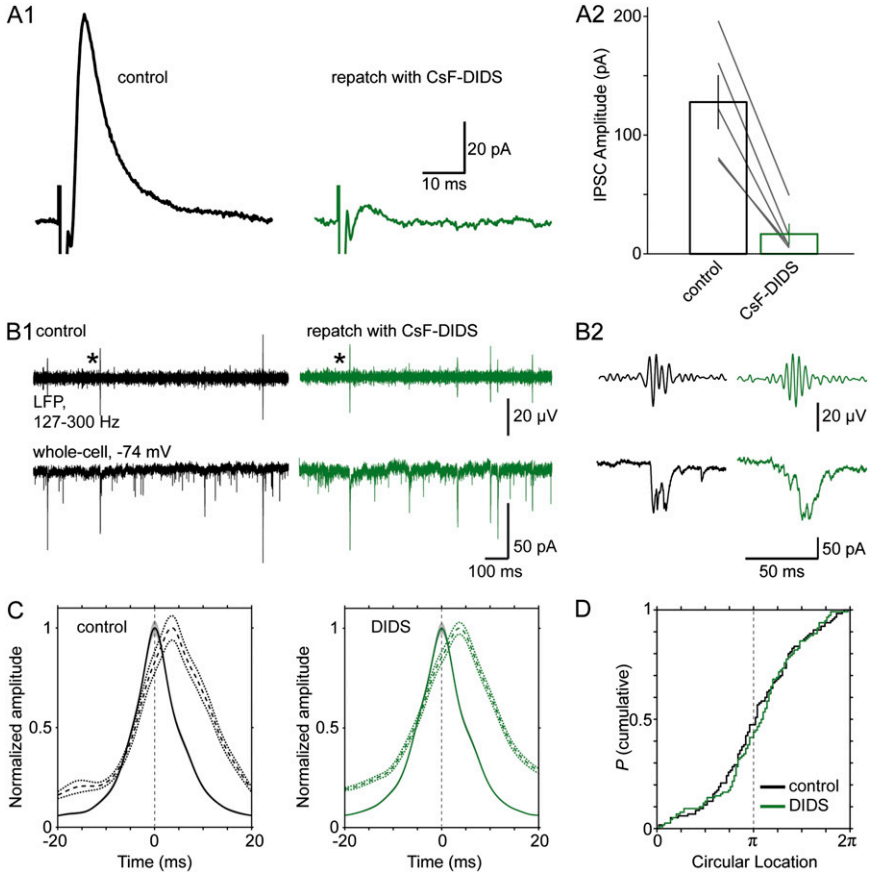

Fig. S5. CsF-DIDS recordings confirmed the excitatory nature of ripple-locked input to O-LM neurons. (*A1 Left*) To demonstrate the intracellular block of postsynaptic inhibition, pharmacologically isolated, stimulus-evoked IPSCs were established (20 μM NBQX, 50 μM D-APV and 20 μM SCH50911 present in the extracellular medium, to block AMPA/kainate, NMDA, and $GABA_B$ receptors). (*Right*) After repatch of the same O-LM cell with 1 mM CsF-DIDS, IPSCs were largely reduced. (*A2*) Summary plot demonstrating CsF-DIDS-mediated reduction of IPSCs (control: 127.8 ± 22.8 pA; CsF-DIDS: 16.7 ± 8.3 pA; 13% of control; $P = 0.008$; rank-sum test; five cells). (*B*) Ripple-associated postsynaptic currents persisted upon repatch-perfusion of O-LM neurons with 1 mM CsF-DIDS (>10-min perfusion time; *B1*, example traces for control and repatch conditions; *B2*, magnification of the marked events). (*C*) Average envelopes of ripples (continuous line) and conductances (dashed line) for control (*Left*) and after perfusion with CsF-DIDS (*Right*). Gray shades and dotted lines represent the SEM. Mean values of delay between peaks: 2.5 ± 0.4 ms and 3.0 ± 0.5 ms. (*D*) Cumulative probabilities plotted for cPSC-to-ripple phases before (black) and after CsF-DIDS perfusion (green; not different, $P = 0.1$, Kuiper's test). Mean vector angles and vector strengths: 189°; 0.43 (control), and 204°; 0.41 (DIDS).

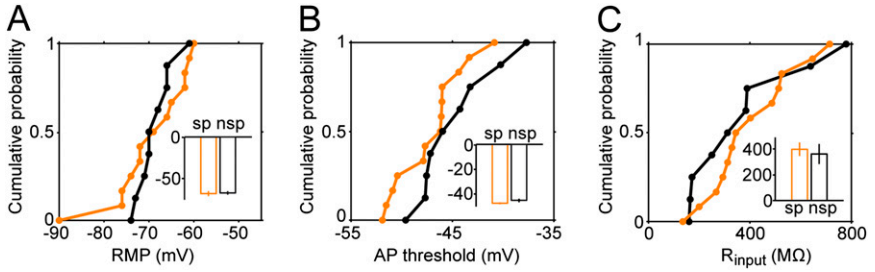

Fig. S6. Ripple-activated and silent O-LM neurons were not different with respect to intrinsic cellular properties. (*A*) Distribution of resting membrane potentials (RMPs) for spiking (orange, median: −69 mV) and nonspiking O-LM neurons (black, median: −70 mV; not different, $P = 0.75$, K–S test). The bar graph (*Inset*) represents the mean values −69.6 ± 2.3 mV and −68.8 ± 1.3 mV for spiking (sp) and silent (nsp) cells, respectively. (*B*) Distribution of action potential thresholds for spiking cells (orange, median: −46.2 mV), and silent cells (black, median: −46.0 mV; not different, $P = 0.44$, K–S test). Mean values are displayed in the bar plot (*Inset*; −47.2 ± 0.3 mV vs. −44.8 ± 0.4 mV). (*C*) Distribution of input resistances (R_{input}) for spiking vs. silent O-LM neurons (medians: 344 MΩ vs. 311 MΩ; not different, $P = 0.68$, K–S test). (*Inset*) The mean values (spiking vs. silent cells: 397 ± 47 MΩ vs. 361 ± 73 MΩ).

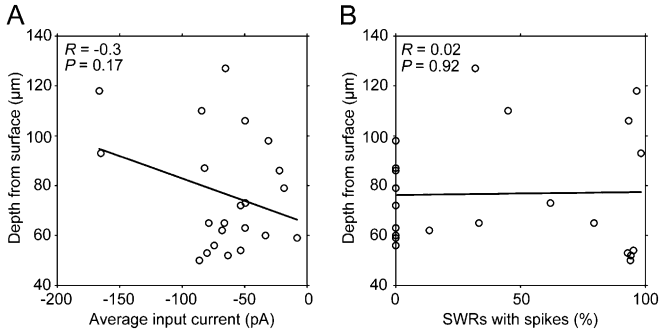

Fig. S7. During SWRs, the average synaptic input current (*A*) and the spiking probability of O-LM cells (*B*) were not correlated with the depth of the cell below the surface of the slice ($n = 22$ cells for both *A* and *B*).

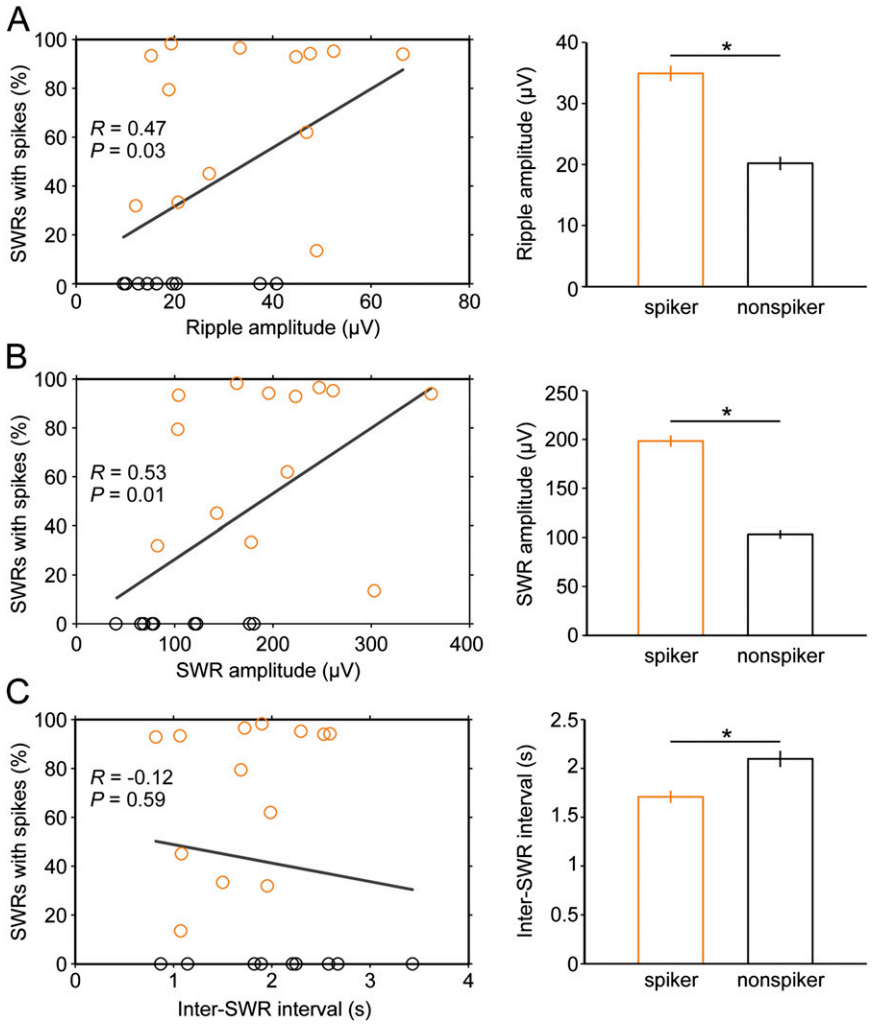

Fig. S8. Summary of SWR characteristics in spiking and silent O-LM neurons derived from cell-attached experiments. (*A Left*) The percentage of SWRs associated with spikes as a function of ripple amplitude (moderate positive correlation; $R = 0.47$; $P = 0.03$; 22 experiments). (*Right*) The mean values of ripple amplitude for spiking and nonspiking O-LM neurons (34.9 ± 1 μV vs. 20.2 ± 1 μV; $P = 2.8 \times 10^{-18}$; rank-sum test; 22 experiments). (*B Left*) Percentage of SWRs associated with spikes as a function of SWR amplitude; both quantities are moderately positively correlated ($R = 0.53$; $P = 0.01$). (*Right*) Mean values of SWR amplitudes for spiking and nonspiking O-LM neurons (198.4 ± 5.8 μV vs. 103.3 ± 4.4 μV; $P = 5.2 \times 10^{-28}$; rank-sum test; 22 experiments). (*C Left*) Percentage of SWRs associated with spikes as a function of the mean inter-SWR interval (no correlation; $R = -0.12$; $P = 0.6$; 22 experiments). (*Right*) Mean values of the inter SWR-intervals for spiking vs. nonspiking neurons (1.7 ± 0.1 s vs. 2.1 ± 0.1 s; $P = 5.0 \times 10^{-5}$; rank-sum test; 22 experiments).